

# Extended X-ray absorption fine structure spectroscopy of selenium-hyperdoped silicon

Bonna K. Newman,<sup>1,a)</sup> Elif Ertekin,<sup>1,b)</sup> Joseph T. Sullivan,<sup>1</sup> Mark T. Winkler,<sup>1,c)</sup> Matthew A. Marcus,<sup>2</sup> Sirine C. Fakra,<sup>2</sup> Meng-Ju Sher,<sup>3</sup> Eric Mazur,<sup>3</sup> Jeffrey C. Grossman,<sup>1</sup> and Tonio Buonassisi<sup>1,d)</sup>

<sup>1</sup>*Massachusetts Institute of Technology, Cambridge, Massachusetts 02139, USA*

<sup>2</sup>*Advanced Light Source, Lawrence Berkeley National Laboratory, Berkeley, California 94720, USA*

<sup>3</sup>*Harvard University, Cambridge, Massachusetts 02138, USA*

(Received 8 August 2013; accepted 10 September 2013; published online 4 October 2013)

Silicon doped with an atomic percent of chalcogens exhibits strong, uniform sub-bandgap optical absorptance and is of interest for photovoltaic and infrared detector applications. This sub-bandgap absorptance is reduced with subsequent thermal annealing indicative of a diffusion mediated chemical change. However, the precise atomistic origin of absorptance and its deactivation is unclear. Herein, we apply Se K-edge extended X-ray absorption fine structure (EXAFS) spectroscopy to probe the chemical states of selenium dopants in selenium-hyperdoped silicon annealed to varying degrees. We observe a smooth and continuous selenium chemical state change with increased annealing temperature, highly correlated to the decrease in sub-bandgap optical absorptance. In samples exhibiting strong sub-bandgap absorptance, EXAFS analysis reveals that the atoms nearest to the Se atom are Si at distances consistent with length scales in energetically favorable Se substitutional-type point defect complexes as calculated by density functional theory. As the sub-bandgap absorptance increases, EXAFS data indicate an increase in the Se-Si bond distance. In specimens annealed at 1225 K exhibiting minimal sub-bandgap absorptance, fitting of the EXAFS spectra indicates that Se is predominantly in a silicon diselenide (SiSe<sub>2</sub>) precipitate state. The EXAFS study supports a model of highly optically absorbing point defects that precipitate during annealing into structures with no sub-bandgap absorptance. © 2013 AIP Publishing LLC. [<http://dx.doi.org/10.1063/1.4824279>]

## I. INTRODUCTION

The optical properties of silicon can be altered by high concentrations of dopant atoms.<sup>1–7</sup> Concentrations of chalcogen atoms (sulfur, selenium, and tellurium) orders of magnitude above equilibrium solid solubilities in silicon can be achieved using a femtosecond laser to dope the substrate from an ambient dopant source.<sup>4,6,8,9</sup> After doping, the silicon exhibits near unity sub-bandgap absorptance out to at least 2500 nm.<sup>1,3–5,7–9</sup> This suggests that optical hyperdoping—the introduction of dopants at high concentrations with pulsed lasers—may be a method to tailor the band structure of Si to engineer properties for enhanced photovoltaic or infrared detector applications.<sup>10,11</sup>

Multiple studies have examined the thermodynamic and optoelectronic properties of this hyperdoped material to understand the nature of the sub-bandgap absorptance<sup>12–15</sup> and have shown that the dopants can be manipulated through thermal processing to engineer optical and electronic properties.<sup>12,14</sup> However, the dopant chemical state and its

evolution during annealing remains unknown, limiting the potential defect engineering of this material.

After optical hyperdoping, the concentration of chalcogen dopants is approximately one atomic percent in the top 300 nm of the surface of the material. Directly probing the dopant structure in this layer is difficult because of the small absolute number of atoms. For many bulk structural probe techniques (i.e., X-ray diffraction, Raman spectroscopy, or Fourier transform infrared spectroscopy), the ratio of dopant signal to noise from the silicon substrate is small. Other techniques such as Auger spectroscopy are limited to only the surface layers up to 20 nm. Synchrotron-based X-ray absorption spectroscopy (XAS) is an element-specific measurement technique<sup>16</sup> that probes the full thickness of the doped layer.

We perform Se K-edge X-ray absorption fine structure (EXAFS) spectroscopy on selenium-hyperdoped samples (Si:Se) to probe the chemical neighborhood of Se atoms, and use density functional theory (DFT) calculations to find favorable (low formation energy) structures to guide the EXAFS structural state analysis. Investigation via EXAFS of a series of samples with varying amounts of sub-bandgap absorptance demonstrates a correlation between sub-bandgap absorptance and the chemical state of the dopant Se atoms. EXAFS spectra indicate that a high fraction of the nearest-neighbors are Si atoms. Further, the distance to these neighbors decreases as the infrared absorptance decreases. Statistical analysis indicates a direct transformation of the chemical state of the Se atoms with the optically non-

<sup>a)</sup>Present address: FOM Institute AMOLF, 1098XG Amsterdam, The Netherlands. E-mail: [bonna@alum.mit.edu](mailto:bonna@alum.mit.edu)

<sup>b)</sup>Present address: University of Illinois, Urbana-Champaign, Illinois, USA. E-mail: [ertekin@illinois.edu](mailto:ertekin@illinois.edu)

<sup>c)</sup>Present address: IBM T. J. Watson Research Center, Yorktown Heights, New York 10598, USA

<sup>d)</sup>Electronic mail: [buonassisi@mit.edu](mailto:buonassisi@mit.edu)

absorbing state well-represented by an early stage SiSe<sub>2</sub> precipitate. EXAFS analysis does not unambiguously identify the chemical nature of the optically absorbing state, potentially due to multiple chemical state populations. However, analysis indicates nearest-neighbor distances similar to Se point defects as calculated by density functional theory. Precise control of the optically active state would allow for efficient engineering of hyperdoped Si:Se materials for specific optical applications.

## II. METHODS

A set of selenium-doped samples was prepared with varying infrared absorptances for synchrotron-based microprobe measurements. We used *p*-type silicon (100) wafers ( $\rho = 3 \text{ k}\Omega\text{-cm}$ ) cleaned with standard semiconductor cleans to remove organic contaminants. We thermally evaporated a 65-nm selenium film (99.95%) onto the wafer before loading onto a translation stage in a stainless steel vacuum chamber. After evacuating to 0.001 Pa, the chamber was back-filled with N<sub>2</sub> to  $6.7 \times 10^4 \text{ Pa}$ . We irradiated the wafers with 80-fs, 800-nm Ti:Sapphire laser pulses. The laser pulses have average energy of 1.7 mJ and are focused to  $590 \mu\text{m}$  (fluence =  $4 \text{ kJ/m}^2$ ) for selenium doping. A  $20 \times 40 \text{ mm}^2$  area was irradiated by translating the sample; and as a result, on average 88 pulses were incident at any point on the scanned area. After irradiation, secondary ion mass spectrometry (SIMS) and elemental analysis with a tunneling electron microscope (TEM) revealed that the top 300 nm of the surface of the silicon substrate is hyperdoped with Se with a concentration between  $10^{20}$  and  $10^{21} \text{ cm}^{-3}$ . Further characterization was carried out using Raman spectroscopy, scanning electron microscopy, and transmission electron microscopy,<sup>17,18</sup> to determine the nature of the surface texturing and dopant incorporation, and confirm a minor presence of secondary silicon phases. The surface is also transformed into a rough landscape of micrometer sized spikes. The details of the doping and resultant structure are described elsewhere.<sup>1,4,8</sup>

After laser doping, the sample was cut into smaller pieces and each piece was annealed for 30 min at temperature between 600 K and 1225 K in a tube furnace in N<sub>2</sub> ambient atmosphere and air cooled to room temperature. While the as-irradiated samples exhibit broad, featureless sub-bandgap optical absorptance, thermal annealing of these hyperdoped samples results in a decrease of infrared absorptance with increased annealing temperature.<sup>12</sup> Applying this thermal processing, we prepare seven samples of varying sub-bandgap absorptance, averaged over wavelengths between 1250–2500 nm, ranging from near 100% to less than 20%. One piece was not annealed (NA) and retains the as-irradiated characteristics. Absorptance was measured with a Hitachi spectrophotometer with an integrating sphere. Transmission (*T*) and reflection (*R*) were measured between the wavelengths of 400 and 2500 nm. Absorptance is calculated as  $A = 1 - R - T$  at each wavelength.

In EXAFS experiments, relative absorption of a beam of coherent X-rays focused on the sample is measured. The X-rays energy is scanned across the absorption edge corresponding to the excitation of a core-shell electron of a

specific atomic species. In this experiment, we use the Se K-edge transition, 12.66 keV. Structural information is observed as perturbations on the absorption signal according to the EXAFS equation<sup>16</sup>

$$\chi(k) = S_0^2 \sum_j \frac{N_j f_j(k) \exp(-2k^2 \sigma_j^2)}{kr_j^2} \sin(2kr_j + \delta_j(k)), \quad (1)$$

where *j* indicates shells of like atoms,  $S_0^2$  is the passive electron reduction factor,  $N_j$  is the coordination number of atoms in each shell, *k* is the photoelectron wavenumber, *r* is the distance to the neighboring atoms, and  $\sigma_j^2$  is mean-square disorder of neighbor distance. The scattering amplitude,  $f_j(k)$ , and the phase shift,  $\delta_j(k)$ , are dependent on the atomic mass of the scattering atoms making Eq. (1) sensitive to the elemental identity of the scattering atoms. Using this equation implemented in the Athena and Artemis (FEFF8) software package,<sup>19,20</sup> we perform non-linear least square fitting of the absorption data to theoretical structural atomic models to extract chemical neighborhood information.

EXAFS experiments were carried out at the Lawrence Berkeley National Laboratory's Advanced Light Source on Beamline 10.3.2 (Ref. 21) using a two Si(111) crystal monochromator with adjustable pre-monochromator slits. The incoming X-ray intensity ( $I_0$ ) is measured in an ion chamber and the fluorescence emission with a seven element LN<sub>2</sub> cooled Ge solid state detector (Canberra) using XIA electronics. To increase surface sensitivity, the samples are arranged at less than a 5° angle of incidence for the incoming X-ray beam, resulting in a cross sectional area of the beam of  $170 \times 7 \mu\text{m}^2$  on the surface of the sample. At this angle, we probe approximately the top 20  $\mu\text{m}$  of material with an effective concentration of Se of  $10^{19} \text{ cm}^{-3}$ .

Using software developed at Beamline 10.3.2, each spectra are corrected for detector dead-time, calibrated for energy using the known spectrally dependent glitches in the monochromator crystal, and any detector element affected by large Bragg reflections from the substrate is removed from the average signal. Multiple scans are averaged together to achieve more than  $10^6$  effective counts (signal/noise basis) at each energy. To analyze the perturbations in absorption that indicate the fine structure, we process the raw absorption signal using a typical EXAFS analysis as outlined elsewhere.<sup>16</sup> After calibrating the energy scale, we use a piece-wise spline fit to the data to remove the background signal and isolate the perturbations due to photoelectron scattering events. For this, we use the AUTOBK function in Athena<sup>19,20</sup> with a background cutoff frequency parameter of  $R_{\text{bkg}} = 1.0 \text{ \AA}$ , which eliminates high frequency noise in the signal. After background removal, the data are normalized and flattened to correct for any slow temporal changes in incoming X-ray intensity. The data are then transformed from energy space to *k*-space (photoelectron wavenumber) through the direct relationship

$$k = \sqrt{\frac{2m(E - E_0)}{\hbar^2}}, \quad (2)$$

where  $E_0$  is the Se K-edge absorption energy. Finally, in order to enhance the signal from higher *k*-space regions and

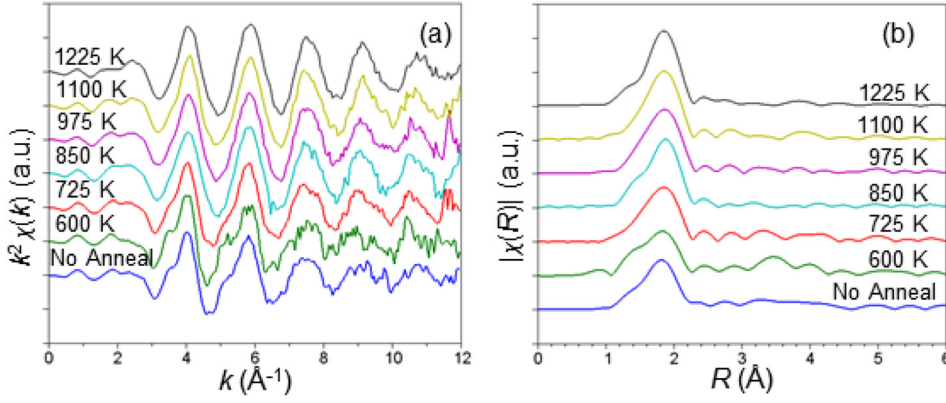


FIG. 1. EXAFS spectra for all seven samples annealed at different temperatures. Spectra are offset for clarity. The  $k^2\chi(k)$  spectra (a) show a smooth variation in the features at  $k = 3.7 \text{ \AA}^{-1}$  and  $4.2 \text{ \AA}^{-1}$ . The data are forward Fourier transformed with a Kaiser-Bessel window from  $k = 1.9 - 11.4 \text{ \AA}^{-1}$  and is shown in (b).

compensate for amplitude decay, we weight the entire spectrum by  $k^2$ .

To calibrate the energy, we collect a full EXAFS spectrum on a red selenium (elemental) standard. Using the known absorption edge, we can calibrate the energy scale. Using Artemis, we perform a two shell fit of the structure of this metallic Se data to a known Se metal structure yielding an absorption edge energy shift,  $\delta E$ , of 4.24 eV and a  $S_0^2$  of 0.95 to be used in fitting the experimental data.

To identify candidate configurations in both the non-annealed and the annealed states, total energy electronic structure methods based on density functional theory<sup>22,23</sup> were utilized. The formation energies of a variety of interstitial and substitutional selenium defects were calculated. All density functional theory calculations reported here are conducted within the generalized gradient approximation (GGA-PBE) to the exchange correlation potential<sup>24</sup> as implemented within the SIESTA software package.<sup>25,26</sup> Troullier-Martins pseudopotentials<sup>27</sup> were used to represent the inner core electrons around each atomic nucleus. The Kohn-Sham orbitals are expanded in a localized, triple-zeta polarization Gaussian basis set that has been obtained via line optimization for silicon and selenium elemental solids. The predicted lattice constant for pure silicon is 5.48 Å in comparison to the experimental value of 5.43 Å, and for hexagonal selenium is  $a = 4.40 \text{ \AA}$  and  $c/a = 1.16$  in comparison to  $a = 4.37 \text{ \AA}$  and  $c/a = 1.14$ . In both cases, the lattice constants are overestimated, as expected for DFT-PBE calculations. The predicted band gap of silicon is 0.70 eV (exp. 1.1 eV), and for selenium is 0.85 eV (exp 1.8 eV); both underestimate the gap in a manner that is typical of conventional DFT calculations.<sup>28,29</sup> For each defect configuration considered, we use 216 atom supercells ( $3 \times 3 \times 3$  supercell of the conventional 8 atom unit cell) and relax all internal atomic coordinates so that forces on the atoms are within 0.01 eV/Å. We have ensured accurate sampling of the Brillouin zone via  $k$ -point convergence; all results reported here are converged to the number of significant figures shown.

### III. RESULTS AND ANALYSIS

Figure 1(a) shows the processed EXAFS spectra ( $k^2\chi(k)$ ) of all seven samples. We note that there is no measurable shift in the absorption edge between samples. However, features at  $k = 3.7$  and  $4.2 \text{ \AA}^{-1}$  vary smoothly

across the data set. This is suggestive of a continuous evolution of chemical state of the Se atoms.

For further analysis, we Fourier transformation (FT) of the  $k^2$ -weighted spectra data with a Kaiser-Bessel window as a bandpass filter to enhance the signal to noise of the data defined from  $k = 1.9 - 11.4 \text{ \AA}^{-1}$ . The resulting spectra, plotted as the magnitude,  $|\chi(R)|$ , are shown in Fig. 1(b). The first large peak in the spectrum is indicative of the signal from the first shell of atoms. Similar smooth evolution of state as seen as an increase in the amplitude of the first shell is observed in the FT spectra.

We also note in Fig. 1(b), a decrease in the amplitude of  $|\chi(r)|$  from higher order shells ( $R > 3 \text{ \AA}$ ) with increased annealing temperature. As the signal is a superposition of the photoelectron scattering functions for each shell, this suggests that in the highly annealed sample, the nearest-neighbors around the Se atoms are well defined but the outer atomic shell structure is more disordered.

In order to describe these states more precisely, we statistically analyze the evolution of the spectra as the annealing temperature increases and sub-bandgap absorptance decreases. Principal component analysis (PCA) is a model-free method of establishing a minimum basis set of component spectra to describe a set of many spectra without losing any significant information.<sup>30,31</sup> PCA is performed on the  $k^2\chi(k)$  spectra in Fig 1(a) with two components. Addition of a third component results in an increase in the Malinkowski indicator, suggesting that two states are sufficient to describe this system.<sup>32</sup> Given a two component system, iterative target factor analysis (ITFA)<sup>33</sup> assigns the identity of component A to be highly correlated to the spectra from the lowest temperature annealed

TABLE I. Results of iterative target factor analysis of  $k^2\chi(k)$  data set using WinXAS.

Annealing Temp. (K)	Comp. A	Comp. B	St. Dev. of fit
No Anneal	0.733	0.267	0.060
600	0.999	0.001	0.03
725	0.589	0.410	0.04
850	0.229	0.770	0.04
975	0.185	0.814	0.03
1100	0.119	0.881	0.02
1225	0.000	1.000	0.02



sample (600 K) and component B to the highest temperature annealed sample (1225 K) as shown in Table I.<sup>34</sup> The ITFA results also suggest that a low-temperature anneal at 600 K acts to purify the sample into component A or the optically active state. This correlates to a small increase in sub-bandgap absorbance after this initial low temperature anneal as seen in Fig. 6.

To explore the chemical state of the first shell in more depth, we isolate the first peak in the FT spectra from  $R = 1\text{--}3\text{ \AA}$  and perform a reverse Fourier transform (RFT) into  $q$ -space. The real part of the RFT spectra ( $\text{Re}(q^2\chi(q))$ ) of the first peak are seen in Fig. 2, revealing isosbestic points at  $q = 8.1, 8.8$ , and  $9.7\text{ \AA}^{-1}$ . The existence of such isosbestic points further supports that the system may be described as a mixture of two end-members in varying proportions. This mixture may be on an atomic basis, such that each Se atom has two sets of neighbors, or such that some Se atoms are in one environment and some in the other.<sup>35</sup> This does not rule out the existence of more than two chemical states for the Se atoms but suggests that the majority of atoms are undergoing the same two-step chemical state transformation with no intermediate chemical state dominating at intermediate temperatures. This is indicative of a balance of equilibrium chemical states determined by thermal history.

We analyzed the EXAFS measurements from the two endpoints of the chemical transformation as indicated by ITFA; the 1225 K annealed sample and the 600 K annealed sample. We will start by discussing the 1225 K annealed sample which has the least sub-bandgap response.

### A. Fitting to annealed state

The EXAFS spectra of the high temperature annealed (1225 K) sample exhibit very little structure past the first shell (Fig. 1). This could be the result of either destructive interference or lack of longer-range order in the second-neighbor shell. The compound  $\text{SiSe}_2$ , an *Ibam* structure with a backbone of Si atoms,<sup>36</sup> is the only known stable room temperature compound state of Si and Se.<sup>37</sup> In this structure,

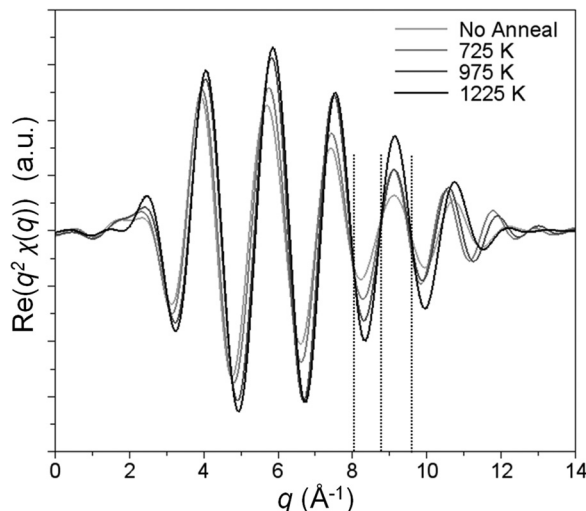


FIG. 2. Overlay of reverse Fourier transformed data from  $R = 1\text{--}6\text{ \AA}$ . We observe isosbestic points at  $q = 8.1, 8.8$ , and  $9.6\text{ \AA}^{-1}$ . Not all spectra are shown for clarity.

Se atoms are bonded to two nearest-neighbor silicon atoms at a distance of  $2.275(1)\text{ \AA}$ .<sup>36</sup> Using Artemis,<sup>19</sup> we fit the first strong peak in the Fourier transformed EXAFS spectra from  $R = 1\text{--}3\text{ \AA}$  to  $1.8\text{ Si}$  atoms at a distance of  $2.292(6)\text{ \AA}$  strongly matching the geometry of this precipitate. In a well ordered crystal of  $\text{SiSe}_2$ , the isolated chains would align with Van der Waals forces. However, previous EXAFS experiments of Si-Se compounds<sup>38</sup> found that crosslinking between the separate chains often occurs such that the system is less ordered and behaves like a glassy substance. Comparison of the annealed-state EXAFS spectrum with previously measured EXAFS spectra shows strong agreement, as shown in Fig. 3. Given that any  $\text{SiSe}_2$  phase that forms would be constrained by the surrounding Si matrix, we expect that it is unlikely that a glassy substance forms, and more likely that single chains of  $\text{SiSe}_2$  form in isolation. We note the striking structural similarity between these chains and the structures proposed for oxygen-related thermal donors in silicon.<sup>39,40</sup> This also fits the proposed model of the change in sub-bandgap absorbance being determined by diffusion of Se atoms to grain boundaries or other energetically favorable nucleation sites.<sup>12,14</sup>

### B. Fitting to non-annealed state

During laser irradiation, the dopant atoms that become incorporated into the silicon most likely become trapped into an ensemble of point defect configurations. To identify candidate low-energy defect configurations that may be present in our samples before annealing, we begin by computing defect formation energies within DFT for a variety of configurations. For a given defect configuration  $D$  in a particular charge state  $q$ , the defect formation energy is given by

$$\Delta E_{D,q}(E_F, \mu_{\text{Si}}, \mu_{\text{Se}}) = (E_{D,q} - E_{\text{perf}}) + n_{\text{Si}}\mu_{\text{Si}} + n_{\text{Se}}\mu_{\text{Se}} + qE_F, \quad (3)$$

where  $E_{\text{perf}}$  is the DFT-computed energy of the perfect silicon supercell,  $E_{D,q}$  is the DFT-computed energy of the supercell with the defect  $D$  in the charge state  $q$  (where  $q$  is expressed in units of charge of an electron),  $E_F$  is the Fermi level of the system, the chemical potentials  $\mu_{\text{Si}}$  and  $\mu_{\text{Se}}$  indicate the prevailing thermodynamic conditions, and  $n_{\text{Si}}$  and

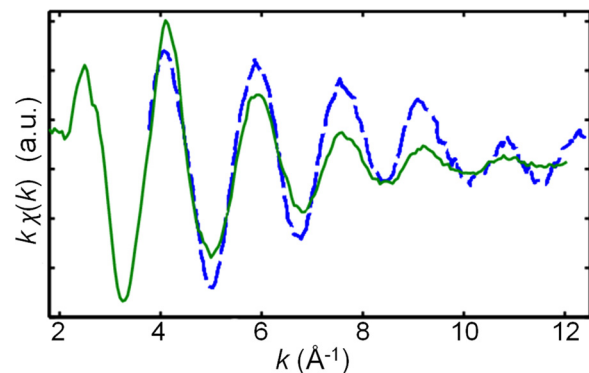


FIG. 3. Comparison of EXAFS data from Ref. 38 of  $\text{SiSe}_2$  chains (dashed) and our fully annealed sample at 1225 K (solid). The two spectra match in phase and location of each peak. The amplitude of each peak can be affected by a number of experimental factors.

TABLE II. Calculated formation energies for the neutral defects ( $q=0$ ). For clarity, schematics of the three most favorable states can be found in Fig. 4.

Configuration	$\Delta E_{D,q}$ (eV)
Substitutional	2.95
Dimer substitutional	3.66
Bond center interstitial	4.69
Offset bond center interstitial	3.54
Tetragonal interstitial	6.14
Hexagonal interstitial	5.47
Vacancy + 2 adj. Se	5.66
Vacancy + 2 opp. Se	5.95

$n_{Se}$  designate the number of Si or Se atoms (respectively) removed from the supercell and added to thermodynamic reservoirs during the defect formation reaction. We use chemical potentials  $\mu_{Si}$ ,  $\mu_{Se}$  corresponding to pure silicon and  $SiSe_2$  chains in equilibrium with each other.<sup>36</sup> The geometries considered include substitutional Se atoms, substitutional Se dimers (in which two adjacent silicon atoms are replaced by two selenium atoms), interstitial selenium atoms in the bond center, offset bond center, hexagonal, and tetragonal configuration, and Se atom—vacancy complexes. A more detailed description of the all of defect complexes is provided in Ref. 41.

Table II shows the calculated formation energies for the neutral defects ( $q=0$ ), which are Fermi-level independent. With no other compensating dopants present to appreciable extent, the Fermi energy of the hyperdoped silicon is expected to remain close to the conduction band edge, favoring defects in the neutral state. We find the lowest-energy defects to be the substitutional Se atom, the substitutional Se dimer, and the offset bond center interstitial Se; for clarity, schematic drawings of these lowest energy defect configurations can be found in Fig. 4. These three configurations remain the most favorable for all values of the Fermi energy. Because defect formation energies computed within conventional DFT are adversely affected by poor description of band gaps, the computed total energies in Eq. (3) are modified in an *ad-hoc* manner by applying a scissors operator to occupied conduction-band-derived defect states when appropriate. Additionally, charged image interactions resulting from the use of periodic boundary conditions are accommodated using a finite supercell extrapolation formalism<sup>42</sup> for the case of charged defects. While these modifications introduce some uncertainty into the computed defect formation energies, we find that the three lowest energy defect configurations remain

unchanged for all reasonable estimates of corrections and modifications. This suggests that, to the extent that thermodynamic equilibrium is applicable, the isolated substitutional, substitutional dimer, and offset bond center interstitial should be the most favorable point defect configuration.

We built FEFF8 atomic models that include all atoms within 6 Å of the central Se atom using the DFT calculated defect structures. We fit the spectra of the non-annealed sample and the 600 K annealed sample to atomic models of the most energetically favorable defect states: Se substitutional, the Se dimer substitutional, and the offset bond center interstitial. The nature of Eq. (1) allows us optimize the fit to each shell ( $j$ ) of atoms separately with  $N_j$ ,  $r_j$ , and  $\sigma_j^2$  as fitting parameters. Initially, we fit to each defect state individually, but we are unable to find reasonable parameters for any of these fits. For the Se substitutional, the number and distance of nearest-neighbors is always smaller and closer, respectively. For the Se dimer substitutional, the nearest-neighbor Se atom does not fit with the data. For the offset bond center interstitial, the distance to the nearest-neighbor Si atoms is much larger than the model and we are unable to fit to a second shell. We also attempt to fit only the first shell of some of the other lower formation energy defects, but find similarly poor fits.

Due to the highly disordered method of dopant introduction, it is possible that all multiple defect states are simultaneously present in the sample. We attempt to fit a combination of the first-shells of the three energetically favorable states. For these fits, we keep the structures fixed but allow each respective component weight to vary. A fit to a combined model of the first shells of the Se substitutional and the offset bond center interstitial yields reasonable parameters but when the second shells are included in the model, the fit is no longer conclusive.

#### IV. DISCUSSION

We now expand the analysis to include the measurements for all annealing temperatures within the context of the two-state transition and end point analysis. To test the hypothesis of an isolated Se point like defect with Si atoms as nearest neighbors, we built two simple models: one with Si atoms and one with Se atoms as nearest neighbors and fit only the first-shell of data ( $R=1-3$  Å) from each sample to these simple atomic models. For all seven spectra, we find better (lower R-factor) fits for nearest-neighbor silicon atoms as opposed to selenium atoms within the fitting window. The fit parameters reject the presence of a Se atom as a nearest-

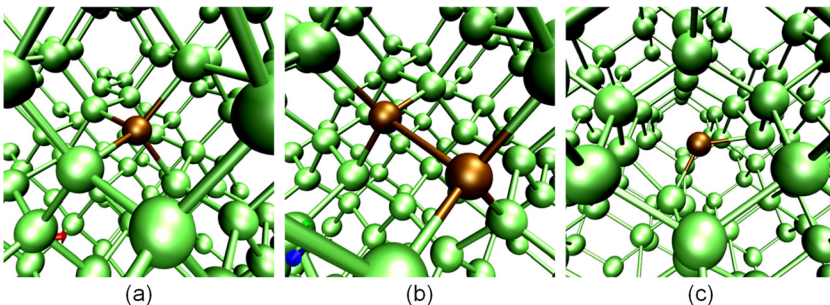


FIG. 4. Structure of the three lowest-energy defects as calculated from DFT: (a) substitutional; (b) dimer substitutional; and (c) offset bond center interstitial defect. Se atoms are marked by darker atoms.

neighbor, suggesting that the Se dimer substitutional and other multi-Se defect states are not likely present in large amounts. While we are unable to uniquely identify the sub-bandgap absorbing defect state, we are able to conclude that the nearest-neighbor is most likely Si atoms and therefore more similar to an isolated Se atom point defect-like state.

The fits are shown in Fig. 5 with corresponding parameter values in Table III. The first-shell fitting to Si nearest-neighbor atoms reveals that for annealing temperatures above 600 K, Se atoms are co-ordinated with an average of approximately two Si atoms. Note that the fits for no anneal and 600 K samples have larger R-factors, suggesting that the simple model of a single Si nearest neighbor is not the uniquely correct fit and that other chemical states are present. As the number of atoms in the fitted shell,  $N_{Si}$ , is a linear scaling factor in Eq. (1), this fitting parameter is often only correct to within 25%.<sup>16</sup> Given this limitation, there is no significant difference in the number of nearest-neighbors as a function of annealing temperature.

The EXAFS equation is sensitive to the nearest-neighbor distance,  $r$ . Fig. 6 shows a correlation between the

TABLE III. Fitting parameters of non-linear least squares fit of the first peak of  $\chi(R)$  spectra from  $R = 1-3$  Å to a model of Si atom nearest-neighbors. The number of nearest-neighbors ( $N_{Si}$ ), average distance to those neighbors ( $r$ ), and the disorder parameter ( $\sigma^2$ ) as noted in Eq. (1) are parameters that are varied in the fit. The R-factor is a representation of the goodness of fit.<sup>19,20</sup> Nearest-neighbor structural data for the most energetically favorable defect structures and structural data for  $\text{SiSe}_2$  are also shown.

EXAFS Fitted Data				
Annealing (K)	$N_{Si}$	$r(\text{\AA})$	$\sigma^2 (\text{\AA}^2)$	R-factor
No anneal	1.65(36)	2.333(11)	0.006(3)	0.110
600	1.75(32)	2.348(12)	0.007(3)	0.121
725	1.69(29)	2.324(7)	0.004(2)	0.070
850	1.76(22)	2.307(5)	0.002(1)	0.039
975	1.86(30)	2.302(7)	0.003(2)	0.064
1100	1.79(27)	2.296(7)	0.002(1)	0.051
1225	1.80(25)	2.292(6)	0.002(1)	0.046
Known structures				
Substitutional	4	2.54	...	...
Dimer substitutional	3	2.42	...	...
Offset bond center interstitial	2	2.26	...	...
$\text{SiSe}_2$ (Ref. 36)	2	2.27	...	...

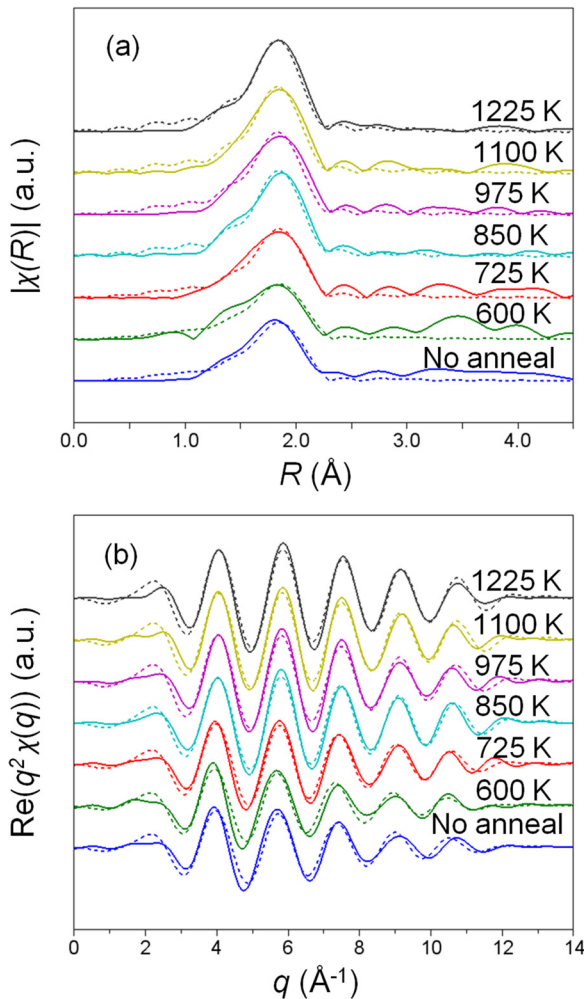


FIG. 5. Fits of the nearest-neighbor peak ( $R = 1-3$  Å) of annealed selenium-hyperdoped silicon samples to a simple atomic model of Si atoms. Solid lines are measured data and dashed lines represent the fits. (a) shows magnitude of  $\chi(R)$  and (b) the real part of the reverse Fourier transform (reverse FT window:  $R = 1-3$  Å, Kaiser-Bessel) in  $q$ -space.

sub-bandgap absorptance and the nearest-neighbor distance; it decreases from around 2.34 Å to 2.29 Å as the annealing temperature increases and the sub-bandgap absorption decreases, the Se atoms, on average, form closer bonds to Si nearest neighbors. Both the single substitutional and dimer substitutional defect states have average distances longer than the  $\text{SiSe}_2$  precipitate. The other lowest energy defect state, the offset bond center interstitial, has a nearest-neighbor bond length comparable to the precipitate. The trend in nearest-neighbor distance seen in the EXAFS spectra suggests that the Se atoms relax from super-saturated substitutional-type defects into precipitated  $\text{SiSe}_2$  states. The corollary decrease in average sub-bandgap absorptance suggests that the substitutional-type defects states may play a key role in the absorption mechanism, as has been suggested by other studies.<sup>12,15</sup> In order to verify this, samples with a

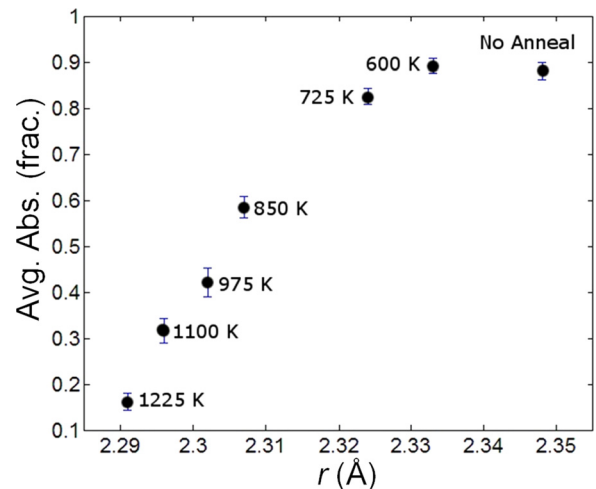


FIG. 6. Average sub-bandgap absorptance between 1250–2500 nm as a function of nearest-neighbor distance as found from EXAFS fitting.



known, specific defect state would need to be prepared and the absorptance analyzed for comparison.

## V. CONCLUSION

EXAFS is performed on a series of Si:Se optically hyperdoped samples that have been annealed to achieve varying amounts of sub-bandgap absorptance to probe the structural nature of observed sub-bandgap absorptance. Analysis of the EXAFS spectra reveals a strong correlation between the Se chemical neighborhood and the magnitude of optical sub-bandgap absorptance measured. The EXAFS spectrum of the non-absorbing state matches the spectrum of SiSe<sub>2</sub> precipitates. Unique identification of the absorbing state is more difficult. We calculate a number of likely theoretical chemical structures and the formation energies of different charge states compared to the SiSe<sub>2</sub> precipitate state. We find the single substitutional, the dimer substitutional, and an offset bond center interstitial are the most energetically favorable configurations. We are unable to find unique fit of the EXAFS spectra for the sample with maximum sub-bandgap absorptance to any simple atomic model, suggesting a possible combination of defects or possibly an unknown structural state. The spectra indicate that the nearest-neighbor atoms are likely two Si atoms. The distance to the nearest-neighbor Si atoms decreases with sub-bandgap absorptance. The longer nearest-neighbor distance corresponding to enhanced sub-bandgap absorptance is in better agreement with distances for the theoretically calculated Se substitutional point defect configurations. The shorter distance is in agreement with the structure of the SiSe<sub>2</sub> precipitated state. The EXAFS analysis supports the model of super-saturated, optically absorbing, isolated Se point defects that precipitate at grain boundaries or other segregation centers during annealing, leading to decreased sub-bandgap absorptance.

Optical doping with pulsed lasers offers the ability to tailor properties of materials through hyper-doping. However, specific control of the chemical state of the introduced dopant will be necessary to achieve optimal properties. This can be achieved both in the introduction of the dopant and by subsequent processing steps. The mid-range chemical structure state reveals that the chemical state of the Se atoms in a point defect like structure is directly correlated to the sub-bandgap absorptance. Knowledge of this chemical state can lead to enhanced control and engineering of sub-bandgap absorptance in silicon for infrared detectors and high-efficiency photovoltaics.

## ACKNOWLEDGMENTS

We gratefully acknowledge Bruce Ravel for assistance with fitting of the EXAFS data. This research was supported by the Chesonis Family Foundation, the National Science Foundation (NSF), and the Department of Energy (DOE) under NSF CA Nos. EEC-1041895, and CBET 0754227, and CHE-DMR-DNS 0934480. B.K.N. acknowledges support from the Claire Boothe Luce Family Foundation. The Advanced Light Source is supported by the Director, Office

of Science, Office of Basic Energy Sciences, US Department of Energy under Contract No. DE-AC02-05CH11231. We also acknowledge the Center for Nanoscale Systems at Harvard University, which is a member of the National Nanotechnology Infrastructure Network (NNIN) that is supported by the NSF under Award No. ECS-0335765.

This document was prepared as an account of work sponsored by the United States Government. While this document is believed to contain correct information, neither the United States Government nor any agency thereof, nor the Regents of the University of California, nor any of their employees, makes any warranty, express or implied, or assumes any legal responsibility for the accuracy, completeness, or usefulness of any information, apparatus, product, or process disclosed, or represents that its use would not infringe privately owned rights. Reference herein to any specific commercial product, process, or service by its trade name, trademark, manufacturer, or otherwise does not necessarily constitute or imply its endorsement, recommendation, or favoring by the United States Government or any agency thereof, or the Regents of the University of California. The views and opinions of authors expressed herein do not necessarily state or reflect those of the United States Government or any agency thereof or the Regents of the University of California.

This manuscript has been authored by an author at Lawrence Berkeley National Laboratory under Contract No. DE-AC02-05CH11231 with the U.S. Department of Energy. The U.S. Government retains, and the publisher, by accepting the article for publication, acknowledges, that the U.S. Government retains a non-exclusive, paid-up, irrevocable, world-wide license to publish or reproduce the published form of this manuscript, or allow others to do so for U.S. Government purposes.

<sup>1</sup>R. Younkin, J. E. Carey, E. Mazur, J. A. Levinson, and C. M. Friend, *J. Appl. Phys.* **93**, 2626 (2003).

<sup>2</sup>C. H. Crouch, J. E. Carey, J. M. Warrender, M. J. Aziz, E. Mazur, and F. Y. Génin, *Appl. Phys. Lett.* **84**, 1850 (2004).

<sup>3</sup>M. A. Sheehy, L. Winston, J. E. Carey, C. M. Friend, and E. Mazur, *Chem. Mater.* **17**, 3582 (2005).

<sup>4</sup>M. A. Sheehy, B. R. Tull, C. M. Friend, and E. Mazur, *Mater. Sci. Eng. B* **137**, 289 (2007).

<sup>5</sup>T. G. Kim, J. M. Warrender, and M. J. Aziz, *Appl. Phys. Lett.* **88**, 241902 (2006).

<sup>6</sup>M. Tabbal, T. Kim, J. M. Warrender, M. J. Aziz, B. L. Cardozo, and R. S. Goldman, *J. Vac. Sci. Technol. B* **25**, 1847 (2007).

<sup>7</sup>C. Wu, C. H. Crouch, L. Zhao, J. E. Carey, R. Younkin, J. A. Levinson, E. Mazur, R. M. Farrell, P. Gothoskar, and A. Karger, *Appl. Phys. Lett.* **78**, 1850 (2001).

<sup>8</sup>C. Crouch, J. Carey, M. Shen, E. Mazur, and F. Genin, *Appl. Phys. A* **79**, 1635 (2004).

<sup>9</sup>Y. Liu, S. Liu, Y. Wang, G. Feng, J. Zhu, and L. Zhao, *Laser Phys.* **18**, 1148 (2008).

<sup>10</sup>A. Luque and A. Martí, *Phys. Rev. Lett.* **78**, 5014 (1997).

<sup>11</sup>J. E. Carey, C. H. Crouch, M. Shen, and E. Mazur, *Opt. Lett.* **30**, 1773 (2005).

<sup>12</sup>B. Tull, M. Winkler, and E. Mazur, *Appl. Phys. A* **96**, 327 (2009).

<sup>13</sup>M. T. Winkler, D. Recht, M.-J. Sher, A. J. Said, E. Mazur, and M. J. Aziz, *Phys. Rev. Lett.* **106**, 178701 (2011).

<sup>14</sup>B. K. Newman, M.-J. Sher, E. Mazur, and T. Buonassisi, *Appl. Phys. Lett.* **98**, 251905 (2011).

<sup>15</sup>E. Ertekin, M. T. Winkler, D. Recht, A. Said, M. Aziz, T. Buonassisi, and J. Grossman, *Phys. Rev. Lett.* **108**, 026401 (2012).

- <sup>16</sup>D. C. Koningsberger and R. Prins, *X-Ray Absorption: Principles, Applications, Techniques of EXAFS, SEXAFS, and XANES* (Blackwell Scientific Publications, Eindhoven, The Netherlands, 1988).
- <sup>17</sup>M. J. Smith, Y.-T. Lin, M.-J. Sher, M. T. Winkler, E. Mazur, and S. Gradečak, *J. Appl. Phys.* **110**, 053524 (2011).
- <sup>18</sup>M. J. Smith, M. T. Winkler, M.-J. Sher, Y.-T. Lin, E. Mazur, and S. Gradečak, *Appl. Phys. A* **105**, 795 (2011).
- <sup>19</sup>B. Ravel and M. Newville, *J. Synchrotron Radiat.* **12**, 537 (2005).
- <sup>20</sup>M. Newville, *J. Synchrotron Radiat.* **8**, 322 (2001).
- <sup>21</sup>M. A. Marcus, A. A. MacDowell, R. Celestre, A. Manceau, T. Miller, H. A. Padmore, and R. E. Sublett, *J. Synchrotron Radiat.* **11**, 239 (2004).
- <sup>22</sup>P. Hohenberg and W. Kohn, *Phys. Rev.* **136**, B864 (1964).
- <sup>23</sup>W. Kohn and L. J. Sham, *Phys. Rev.* **140**, A1133 (1965).
- <sup>24</sup>J. P. Perdew, K. Burke, and M. Ernzerhof, *Phys. Rev. Lett.* **77**, 3865 (1996).
- <sup>25</sup>J. M. Soler, E. Artacho, J. D. Gale, A. Garca, J. Junquera, P. Ordejón, and D. Sánchez-Portal, *J. Phys.: Condens. Matter* **14**, 2745 (2002).
- <sup>26</sup>E. Artacho, E. Anglada, O. Díguez, J. D. Gale, A. Garca, J. Junquera, R. M. Martín, P. Ordejón, J. M. Pruneda, D. Sánchez-Portal, and J. M. Soler, *J. Phys.: Condens. Matter* **20**, 064208 (2008).
- <sup>27</sup>N. Troullier and J. L. Martins, *Phys. Rev. B* **43**, 1993 (1991).
- <sup>28</sup>J. P. Perdew, R. G. Parr, M. Levy, and J. L. J. Balduz, *Phys. Rev. Lett.* **49**, 1691 (1982).
- <sup>29</sup>P. Mori-Sánchez, A. J. Cohen, and W. Yang, *J. Chem. Phys.* **125**, 201102 (2006).
- <sup>30</sup>T. Ressler, J. Wong, J. Roos, and I. Smith, *Environ. Sci. Technol.* **34**, 950 (2000).
- <sup>31</sup>A. I. Frenkel, O. Kleinfeld, S. R. Wasserman, and I. Sagi, *J. Chem. Phys.* **116**, 9449 (2002).
- <sup>32</sup>E. Malinowski, *Anal. Chem.* **49**, 612 (1977).
- <sup>33</sup>A. Elbergali, J. Nygren, and M. Kubista, *Anal. Chim. Acta* **379**, 143 (1999).
- <sup>34</sup>B. Newman, J. Sullivan, M. Winkler, M. Sher, M. Marcus, S. Fakra, M. Smith, S. Gradečak, E. Mazur, and T. Buonassisi, in Proceedings of the 24th European Photovoltaic Solar Energy Conference (2009), p. 236.
- <sup>35</sup>IUPAC, *Compendium of Chemical Terminology (The "Gold Book")*, 2nd ed., edited by A. D. McNaught and A. Wilkinson (Blackwell Scientific Publications, Oxford, 2012).
- <sup>36</sup>J. Peters and B. Krebs, *Acta Crystallogr. Sec. B* **38**, 1270 (1982).
- <sup>37</sup>H. Okamoto, *J. Phase Equilib.* **21**, 499 (2000).
- <sup>38</sup>R. Johnson, D. Price, S. Susman, M. Arai, T. Morrison, and G. Shenoy, *J. Non-Crystal. Solids* **83**, 251 (1986).
- <sup>39</sup>D. J. Chadi, *Phys. Rev. Lett.* **77**, 861 (1996).
- <sup>40</sup>J. Coutinho, R. Jobes, L. I. Murin, V. P. Markevich, J. L. Lindström, S. Öberg, and P. R. Briddon, *Phys. Rev. Lett.* **87**, 235501 (2001).
- <sup>41</sup>Y. Mo, M. Z. Bazant, and E. Kaxiras, *Phys. Rev. B* **70**, 205210 (2004).
- <sup>42</sup>N. D. M. Hine, K. Frensch, W. M. C. Foulkes, and M. W. Finnis, *Phys. Rev. B* **79**, 024112 (2009).